*lubricants*

MDPI

*Article*

# Effect of Change in Material Properties of the Abradable Coating on the Wear Behavior of It—Microstructure Model-Based Analysis Approach

**Anitha Kumari Azmeera [1], Prakash Jadhav [1,*] and Chhaya Lande [2]**

[1] Department of Mechanical Engineering, SRM University AP, Amaravati 522240, India; anitha_a@srmap.edu.in
[2] Symbiosis Institute of Technology, Symbiosis International University (Deemed), Pune 412115, India; chhaya.lande@sitpune.edu.in
* Correspondence: prakash.j@srmap.edu.in

**Abstract:** In aerospace applications, engine parts, especially those around the rotor blade tips, are coated with an abradable seal, a specific material layer. Its design produces a tighter seal without harming the blades by allowing it to wear down or "abrade" somewhat when the blade tips come into contact. In turbines and compressors, this reduces gas leakage between high- and low-pressure zones, increasing engine efficiency. Abradable seals are crucial to contemporary jet engines because they enhance performance and lower fuel consumption. The materials selected for these seals are designed to balance durability and abrasion resistance under high temperatures and speeds. Metal matrix, oxide particles, and porosity are the three most prevalent phases. An ideal mix of characteristics, such as hardness and erosion resistance, determines how effective a seal is, and this is accomplished by keeping the right proportions of elements in place throughout production. The primary objective of this research is to optimize abradability by utilizing various FEM tools to simulate the rub rig test and modify testing parameters, including Young's modulus, yield stress, and tangent modulus, to analyze their impact on the wear behavior of the abradable seal and blade. Two microstructure models (CoNiCrAlY–BN–polyester coating) were found to perform optimally at porosity levels of 56% and 46%, corresponding to hardness values of 48 HR15Y and 71 HR15Y, respectively. Changing factors like yield stress and tangent modulus makes the seal more abrasive while keeping its hardness, porosity, and Young's modulus the same. Furthermore, altering the Young's modulus of the shroud material achieves optimal abradability when tangent modulus and yield stress remain constant. These findings provide valuable insights for improving material performance in engineering applications. To improve abradability and forecast characteristics, this procedure entails evaluating the effects of every single parameter setting, culminating in the creation of the best abradable materials. This modeling technique seems to provide reliable findings, providing a solid basis for coating design in the future.

**Keywords:** abradable coating seal (CoNiCrAlY–BN–polyester); abradability; microstructure; compressor; finite element method



Received: 24 November 2024
Revised: 2 January 2025
Accepted: 6 January 2025
Published: 8 January 2025

**Citation:** Azmeera, A.K.; Jadhav, P.; Lande, C. Effect of Change in Material Properties of the Abradable Coating on the Wear Behavior of It—Microstructure Model-Based Analysis Approach. *Lubricants* **2025**, *13*, 22. https://doi.org/10.3390/lubricants13010022



## 1. Introduction

The fixed parts of gas turbines are coated with certain materials called abradables, which are intended to erode more slowly than the blade tips. This controlled erosion also reduces leakage by minimizing clearance and increasing aerodynamic efficiency. Usually made of ceramic or polymeric materials, they offer better wear properties and temperature

resistance. Applications such as aerospace engines and power generation turbines utilize them to enhance performance and prolong component life. Utilizing them is critical to achieving reduced emissions and increased efficiency in hot conditions [1–5]. Abradable coatings play a major role in minimizing the gap between fixed components and revolving blades. This improves the efficiency of the turbine and prevents leakage. When processing abradable seal materials, thermal spraying is the most widely used method. Two techniques used in manufacturing are chemical vapor deposition (CVD), which creates a uniform coating via gas-phase processes, and plasma spray, which melts small particles and sprays them onto a substrate. These procedures allow for precise control of coating characteristics and thickness. The end product is a customized material that strikes a compromise between enough wear resistance and the softness required to wear away during operation [6–8]. Complex wear processes in abradable materials used in aerospace applications, particularly in rotor or blade systems, are caused by high pressures, friction, and temperature variations. Surface erosion, adhesive wear, and oxidation under dynamic loading are the ways in which these materials deteriorate. Variables such as temperature, load, speed, and ambient factors influence their thermodynamic performance. The wear behavior, which includes abrasive micro-cutting, fatigue wear, and material transfer, might eventually affect the component's lifespan. Using high-quality abradable seal coatings increases the reliability of gas turbine blades by protecting them from a variety of failure modes, such as heat exposure, corrosion, fatigue, creep, and high temperatures. In general, this enhances the durability, efficiency, and performance of gas turbine engines used in the aerospace sector [9–12].

Abradable materials, also referred to as engineered coatings, use controlled wear to lower the gap between fixed and rotating parts in high-performance systems like gas turbines. Depending on the application, these materials can consist of metallic coatings such as Ni–Al, polymer-based compounds, or ceramic–metal composites such as Al–Si alloys. To maximize engine efficiency and limit blade damage during contact, because of their low density, resistance to wear, and thermal stability, these materials were chosen [13–15]. By mimicking actual contact between revolving blades and abradable surfaces, the rub rig test method assesses the abradability of coatings in aircraft applications. This experiment involves applying a controlled, high-speed rubbing action from a rotating blade at precise loads, speeds, and temperatures to a stationary sample of the abradable material. A crucial factor in evaluating the efficacy of abradable coatings is abradability, which is defined as the volume loss resulting from shroud wear divided by blade wear. This procedure demonstrates the material's abradability, thermal stability, and impact on the integrity of turbine blades. These experiments typically use steel, titanium alloy, or nickel alloy blades. To assess the performance of abradable coatings under diverse circumstances, testing might also make use of softer materials. In general, abradable coating testing is essential to guaranteeing the material's efficacy in practical applications, including gas turbine engines, since it yields important information on the material's overall performance, wear resistance, and abradability [16–18]. For researching the microstructures of coatings, scanning electron microscopy, or SEM, is a crucial instrument. High-resolution images of the coating's microstructure can be obtained using a powerful SEM equipped with a backscattered electron (BSE) mode. The exact parameters specified, such as a 120 kW power supply at 20 kilovolts, indicate the settings used to obtain the coating's microstructure images. Simulation software uses finite element (FE) models to support experimental observations and provide a deeper understanding of coating behavior. Scientists can use these models to look into how materials behave at high temperatures, how residual stress is distributed, how thermal barrier coating (TBC) breaks, and how bending wear affects composite ceramic coating [19–21]. This is accomplished by modeling how coatings react mechanically and thermally under varied conditions.

The study by Bolelli et al. [22] presents a microstructure-based thermo–mechanical modeling method for thermal spray coatings. It emphasizes examining how the microstructural properties of the coatings relate to their mechanical and thermal performance. In order to forecast how the coatings will behave under diverse mechanical and thermal stressors, this study integrates experimental data with numerical simulations. This study will significantly improve the design and optimization of thermal spray coatings for a range of industrial applications. Nayebpashaee et al. [23] use a finite element simulation to investigate the failure mechanism of plasma-sprayed thermal barrier coatings (TBCs) and the residual stress distribution. By using the coatings' real microstructure as a representative volume, this study simulates stress behavior more accurately. This study shows how microstructure impacts residual stresses and crack formation, which is helpful for understanding how to make TBCs work better and last longer in high-temperature situations. Klusemann et al. [24] focus on microstructure-based modeling of residual stresses in WC-12Co thermal spray coatings. Using numerical simulations, the study examines how coating microstructural characteristics, such as porosity and particle dispersion, impact the formation of residual stress. By incorporating these microstructural characteristics, the model helps understand how stress accumulates and how WC-12Co coatings could fail. This method optimizes coating characteristics to increase lifespan and performance. Sheng et al. investigated the effects of layer count on the wear behavior [25], mechanical characteristics, and microstructure of TiN/Ti multilayer coatings produced by high-power magnetron sputtering. Using the Hall–Petch effect, scientists discovered that increasing the number of layers strengthened the edges between the grains and made the material tougher and more wear-resistant. In addition to increasing adhesion strength, optimized layer numbers also avoided problems like delamination. This research emphasizes how crucial multilayer architecture is for creating long-lasting, high-performing coatings. Zemlianov et al. investigate the effect of bi-layer metal–matrix composite coatings on the mechanical strength of coated materials [26]. This work uses numerical simulations to evaluate the coating's impact on the total material strength and stress distribution under mechanical loading. The results show how the composite coating improves the material's lifespan and load-bearing capacity, offering guidance for the creation of cutting-edge protective coatings for structural applications. Irissou et al. examined the tribological characteristics of CoNiCrAlY–BN abradable coatings sprayed with plasma [27]. Characterizing these commonly used coatings' wear behavior, friction, and abrasion resistance is the main goal of the study in gas turbine applications. The study's experimental testing demonstrates how the microstructure and composition of the coatings impact their performance. This provides valuable information for developing longer-lasting and more effective abradable coatings. Aussavy's Ph.D. dissertation focuses on the processing, characterization, and modeling of the thermomechanical characteristics of three abradable coatings—NiCrAl–bentonite, CoNiCrAlY–BN–polyester [28], and YSZ–polyester. This study investigates the manufacturing process of these coatings, their microstructural characteristics, and their performance under mechanical and thermal stress. Through experimental and modeling methods, this work offers valuable understanding for enhancing these coatings in applications like gas turbines, where abradability and heat protection are crucial. Faraoun et al. [20] present a modeling technique for abradable coatings, focusing on the mechanical and thermal behavior of the coatings in gas turbine applications. The study uses a combination of numerical models and experimental data to predict the performance of these coatings under operating conditions. The model takes into account important variables such as temperature effects, wear resistance, and coating detachment. It provides a valuable understanding of how to design and apply abradable coatings to enhance durability and efficiency. Mittal's book High Performance Polymers and Engineering Plastics [29] provides

a thorough introduction to advanced polymers and their uses in engineering. The book examines the synthesis, characteristics, processing, and performance of high-performance polymers, highlighting their use in challenging environments like electronics, automotive, and aerospace industries. The text also covers the most recent developments in polymer technology, emphasizing the engineering of these materials to enhance their mechanical, thermal, and chemical resistance. In the exploration of abradable coating development using microstructure-based models, Jadhav [30] emphasizes the potential for microstructural engineering to tailor coating performance. This research examines the relationship between material composition, abradability, durability, and microstructure. The study employs sophisticated modeling methods to provide valuable perspectives on coating design optimization for high-performance applications, such as turbines, where precise material removal and effective sealing are critical. A finite element approach based on microstructure images is presented by Azmeera et al. [31] for the design of abradable coatings for aero engines. The study estimates the performance of wear-resistant coatings in practical settings using finite element analysis and high-resolution microstructural imaging. By simulating the influence of microstructural features on coating behavior, this study provides valuable information to enhance coatings' wear resistance, sealing capabilities, and overall engine efficiency in aerospace applications. Huang et al. [32] provide a comprehensive analysis of thermally sprayed abradable sealing coatings, with a focus on the material's abradability. This research investigates the relationship between coating composition, microstructure, and abradability performance as it looks at different kinds of abradable coatings used in gas turbines and aero engines. It also covers the latest developments in coating technologies, the difficulties in reaching ideal abradability, and methods for enhancing these coatings' resilience and sealing effectiveness in hot conditions. Bertuol et al. examine the impact of hexagonal boron nitride (hBN) on the abradable performance of AlSi-based coatings [33]. By examining how adding hBN affects these coatings' wear, friction, and wearability, the study closes the gaps between tribological testing and abradability testing. The research demonstrates how hBN improves coating performance through experimental evaluations, making it more appropriate for high-temperature applications, such as gas turbines, where wear resistance and effective sealing are critical. The focus of Volpe et al. [34] is to enhance brazing procedures for wear-resistant porous FELTMETAL seal materials; they do this by using thermo gravimetric analysis (TGA) and differential scanning calorimetric (DSC) at the same time. The study's goal is to find the best way to braze by looking at how stable the materials are and how they react to heat at high temperatures. In order to increase efficiency and lifespan in challenging conditions, FlexmetalTM seals—which are essential in applications like gas turbines—must perform better when it comes to bonding. Advanced materials that can endure high operating loads while retaining efficiency and safety are required by the aircraft sector. With its ability to provide accurate clearance control, wear resistance, and improved sealing in vital parts like compressors and turbines, abradable materials have become essential. New developments in hybrid nanocomposites, which combine nanoscale reinforcements with metallic matrices, have shown remarkable mechanical and thermal capabilities, which make them perfect for use in aeronautical systems [35]. Tribological coatings that are thermally sprayed enhance wear resistance even further in high-stress settings [36]. In order to improve the design and performance of abradable coatings, computational models such as the micro–macro finite element approach are increasingly used to anticipate the rub reaction [37]. The use of wear-resistant coatings in harsh aerospace environments has also been improved by microstructural assessments [38]. When taken as a whole, these developments demonstrate how important abradable materials are to the advancement of aircraft technology.

Abradable seal coatings play a critical role in enhancing the efficiency and reliability of various engineering systems, particularly in aerospace and industrial applications. Recent advancements have focused on optimizing their microstructure, thermal stability, and wear resistance to meet the demands of high-temperature and high-speed environments. Cui et al. [38] examined the microstructural and phase transformations in DySZ–polyester coatings after thermal exposure, highlighting significant changes that influence their abradability and sealing performance. Similarly, Gao et al. [39] emphasized the importance of balancing thermal and mechanical properties to improve coating performance under high-speed rubbing conditions, underscoring the need for optimized thermal conductivity and wear resistance. Processing parameters also play a crucial role, as demonstrated by Soltani et al. [40], who found that the wear behavior of nickel–graphite coatings at elevated temperatures could be tailored through precise control of Air Plasma Spray (APS) settings.

Temperature's impact on wear mechanisms has also been extensively studied. Martinet et al. [41] explored aluminum-based coatings in dynamic interactions with Ti6Al4V blades, revealing accelerated material degradation at higher temperatures, while Kang et al. [42] introduced porous spheres to enhance high-temperature abradability and operational lifespan. The development of lightweight and flexible coatings, such as the epoxy-based formulations by Tong et al. [43], offers additional benefits, including improved bonding strength and reduced weight, making them ideal for applications like aero-engines. Furthermore, innovative materials like the CuAl–Ni/C seal coating presented by Yan et al. [44] provide dual functionalities of abradability and anti-corrosive properties, which are essential for extending service life in harsh environments.

Material removal mechanisms and their implications for coating design have also been a focus of research. Zhang and Marshall [45] identified abrasion as the primary mode of material loss in Al–Si-based coatings, stressing the importance of design adjustments to minimize wear-related inefficiencies. Criteria for enhancing gas turbine engine performance through optimized coatings were outlined by Mohammad et al. [46], who emphasized the need for improved wear behavior, thermal stability, and adherence. Additionally, broader perspectives on technological advancements were provided by Silva et al. [47], who discussed the integration of abradable coatings into advanced aero-engine systems under the European Project E-BREAK.

The main purpose of this work is to design a simulation method for understanding and predicting coating abradability using microstructure-based image models. The present work is organized as follows: Section 2 discusses the selection of wear-resistant coating materials, as well as the test modeling technique that uses a rub rig to determine the abradability attribute needed to characterize the microstructure. This research focusses on the experimental work that was mentioned, which used plasma spray to apply an abradable powder known as CoNiCrAlY–BN. In this article, we generated a range of coating changes, along with microstructural pictures, porosity and hardness data, and erosion rate measurements. The proposed methodology was validated using experiments from the cited study [27]. Section 3 research emphasizes wear analysis, meshing, and microstructure modelling with different FEM tools [30,31]. These FEM tools allow you to create a microstructure model of an abradable coating and conduct a wear study by testing it on a dummy rub rig. Experimental input data from previously cited studies were utilized in this research [16,28,29,48–54] to verify this methodology. This paper concludes with a summary of key points. Proper design of abradable coatings for turbine blades and housing is crucial, as they seal gaps and shield surfaces from impact. Using a simulation methodology to forecast the properties of coatings can save a significant amount of repetitious experimental effort compared to performing experiments. This research introduces a unique modelling methodology that predicts coating behavior based on a

limited number of microstructure images. If successful, this method can greatly aid in optimizing the design of abradable coatings for improved performance.

## 2. Materials and Methods

### *2.1. Application of Abradable Seal for Aerospace and Its Consideration Condition*

As shown in Figure 1a from [28], Abradable coatings are critical in aerospace engineering, particularly in gas turbine engines and compressors, to enhance efficiency, reliability, and durability. These coatings are applied to sections like turbine and compressor blades, where minimal clearances are essential to reduce air leakage and maximize engine performance. In high-pressure compressors, they enable tighter blade-tip clearances, optimizing operational efficiency despite thermal expansion and mechanical movement. Abradable coatings also create self-adjusting seals, reducing friction and wear on rotating components, which is vital for improving fuel efficiency and lowering maintenance costs. Additionally, they protect blade tips from wear during incidental contact with the casing, ensuring the longevity and reliability of engine components. In hot sections of engines, these coatings provide thermal insulation and oxidation resistance, which are crucial for durability under extreme temperatures. Engines experience enormous centrifugal forces during operation; therefore, the coatings need to be strong enough to withstand delamination and keep their mechanical integrity at high rotational speeds. Furthermore, the material must be resistant to erosion, since airflow-borne particles such as dust and debris can gradually erode seals and reduce their efficiency.

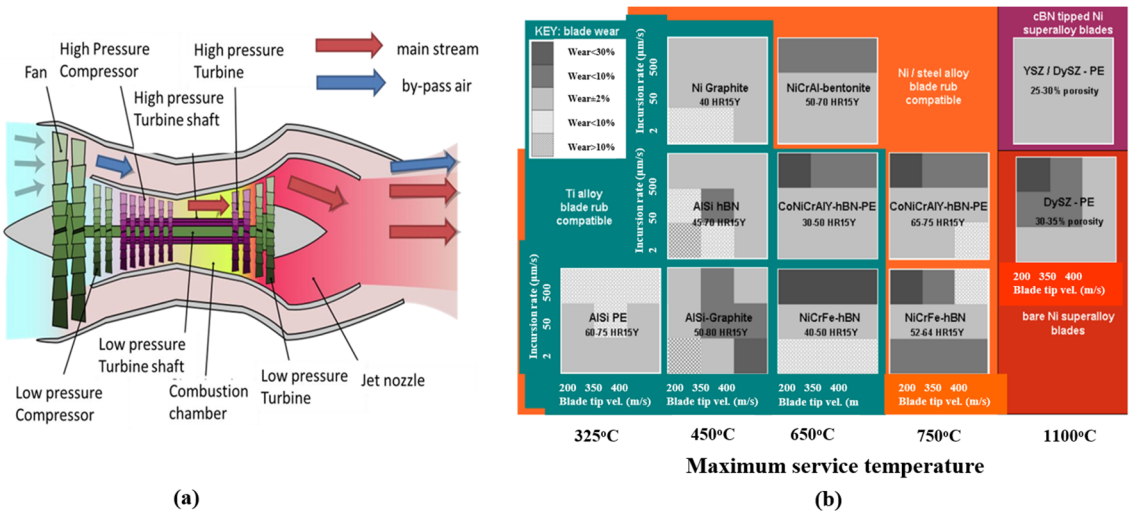


**Figure 1.** (**a**) Engine part locations line diagram [28]; (**b**) a summary of the main abradable coating systems' typical incursion test blade wear measurements at various incursion settings, coating hardness ranges, and blade material compatibility as a function of their maximum service temperatures [51].

Another important consideration is thermal expansion since the stationary components and the moving blades expand at different rates. The abradable material must support this expansion without causing excessive wear or seal failure. Regulating the wear rate is essential to ensure the coating wears down gradually without causing significant leaks throughout the engine's operating life. The coating's capacity to perform under temperature and pressure variations—which are typical in aircraft applications—determines its long-term dependability. Abradable coatings help control blade tip clearance by wearing down somewhat during operation, ensuring that the blades can function well without running the risk of rubbing against the case. Turbine blades continuously rotate across the inner circle of the casing, coating it with materials such as CoNiCrAlY–BN–polyester, NiCrAl–bentonite, and YSZ–polyester, among others, to maintain the distance between the blade and the

housing. Figure 1b presents an overview of typical incursion test measurements, focusing on blade wear under various incursion conditions, compatibility with blade materials, and the hardness range of different abradable coating systems, analyzed as a function of their maximum service temperatures. In these tests, a high-velocity gas stream is used to heat the abradable specimen to the desired temperature, simulating operating conditions. Test blades are mounted on a turbine disc capable of achieving tip speeds of up to 500 m/s. In this research, the boundary conditions relevant to blade interactions with the CoNiCrAlY–BN–polyester abradable coating are defined based on the referenced studies [51], ensuring an accurate representation of real-world turbine behavior. The thermal spray method creates the current clearing seal for the high-pressure turbine.

### *2.2. Experimental Procedure for Sample Production and Microstructure Sample Characterization*

Abradable coating microstructures were used in this study; the APS microstructures in Figure 2a,b were obtained from the literature [27]. The commercially available abradable powder (CoNi–CrAlY–BN) and plasma spray were used. Researchers developed a wide range of microstructural characteristics and attributes in the coating by manipulating the manufacturing conditions. Aircraft and industrial gas turbines use the high-pressure compressor portion. The effects of surface hardness and porosity on wear behavior were examined using (i) erosion and (ii) rub rig tests to replicate the usual service environment. The abradable coating was made from a spray-dried composite powder (SM 2043, Sulzer Metco, Westbury, NY, USA) called CoNiCrAlY–BN–polyester (Co25Ni16Cr6Al0.3Y-4BN-15 polyester (given in weight %); the size of the particles is 176/+11 lm). The exact composition of the CoNiCrAlY alloy used in their study is as follows: 21% cobalt (Co), 25% nickel (Ni), 16% chromium (Cr), 6% aluminum (Al), and 0.3% yttrium (Y). The BN (boron nitride) content in the coatings is approximately 4%. The CoNiCrAlY alloy enhances oxidation resistance and mechanical properties, while the BN phase offers low friction and high wear resistance. In this paper, the mild steel 1020 substrates were grit-blasted with Grit 24 alumina prior to bond coat application. While putting the coatings on and installing the APS torches, the robot moved in a quadratic raster pattern.

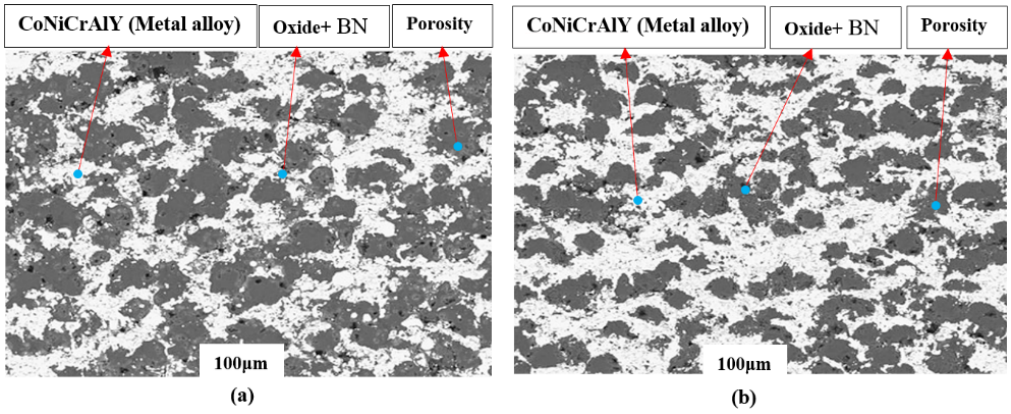


**Figure 2.** (**a**) A total of 56% porosity (48 HR15Y) and (**b**) 46% porosity (71 HR15Y) [27].

This investigation determined the porosity levels required for seals that may wear away by heating the sprayed samples and removing the polyester from the coating. The deployment of an appropriate exhaust system that continuously supplied oxygen enabled the polymer to burn off during the 3.5 h of heat treatment in air at 500 °C. With CoNiCrAlY–BN polyester, APS engineers have produced abrasive coatings with a range of porosities and surface Rockwell hardness. Adhesion, rubbing tire, and eroding wear tests were used to assess the behavior and performance of the coatings. The findings demonstrate that abradable coatings can become harder by decreasing their porosity. The APS microstruc-

tures in Figure 2a,b were taken from the literature and used in the research as abradable coating microstructures [26] for modeling the microstructure.

### *2.3. Rub Rig Test and Modeling Approach for the Configuration of the Rub Rig Test*

The testing of abradable coatings on coupons and blade tips in aerospace applications using mass loss involves precise measurement and analysis. Samples are coated with abradable material, and their initial mass is recorded. The coated samples undergo wear testing in controlled conditions, simulating engine environments through repeated blade interactions. After testing, the mass loss is calculated by comparing pre- and post-test weights, providing insights into the wear behavior and performance of the coatings. The standard references can be found in [52]. The experimental setup used to evaluate coatings' abradability performance is known as the abradable rig test [28,55,56]. The purpose of the rub rig test equipment is to replicate real-world engine conditions and the interaction between rotating turbine blades and abradable coatings based on reference [51]. As shown in Figure 3a, a stationary surface covered in abradable materials like YSZ–polyester, CoNiCrAlY–BN–polyester, and NiCrAl–bentonite is periodically in touch with the blades of a high-speed rotating disc in this configuration. The wheel is rotated rapidly during this test, which wears down the wheel and removes the coating. Important elements like heat generation, friction forces, coating erosion, and blade wear are all monitored by a number of sensors. These measures are essential for evaluating how well the coatings shield the blades from excessive wear while allowing for controlled material removal from the coating.

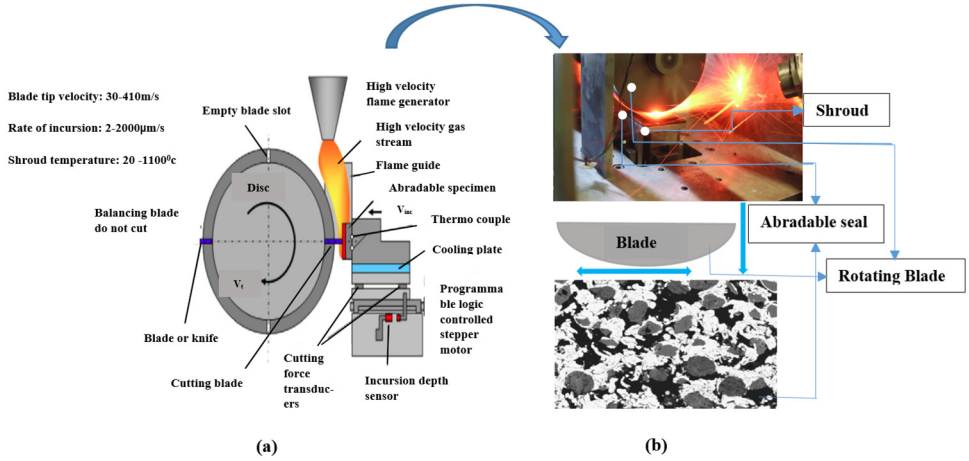


**Figure 3.** (**a**) Oerlikon abradable incursion test facility based in Winterthur, Switzerland [37]; (**b**) the planning of the apparatus for rub rig dynamic wear simulation approach.

Data on coating wear on coupons and blade tip wear are gathered when an experiment is finished. The comparison of the coating's abradability to the wear of the blade enables an assessment of its performance. To accomplish this, attempts were made to simulate the dynamic processes occurring in the blade coating microstructure. Wear on the wheel surface and coating surface was measured based on references [27,37,52,57]; abradability is computed as the ratio of coating wear to wheel wear. An abradability ratio of from 10 to 20 is ideal for a high-quality abradable seal. As shown in Figure 3b the primary method of modelling in this case is the use of 3D FEA models of this configuration with a microstructure-based foundation. Micrography was used to analyze the microstructure of the coating when it was first created on coupons using APS (air plasma spraying). Based on the microstructure photograph, the FEA model and mesh were created using this research. The model and final mesh were created with Autodesk Fusion 360 2021 and Hyper Mesh

2021 software. To simulate dynamic wear, a 3D model of the coating was created, and a microscopy model was simulated by importing the resulting mesh file into the LS-DYNA R11 [48] program for additional processing. Replicating the coating's behavior on a rub rig, as observed in the rub rig test setting, is the main objective of this model. The simulation was adjusted in several ways to simplify the modeling process. Instead of spinning like a wheel, the blade repeatedly moves in the same direction, forward and backward. The blade on the coating microstructure was turned at a speed that was proportionate to the rotating wheel's tangential speed. The abradability was assessed by looking at the blade and microstructure volume loss after the simulation was finished. This test setup guarantees that the results are very relevant to the longevity and performance of turbine engines by replicating the interactions between blades and coatings that occur in the actual world.

### *2.4. FE Modal for 3D Microstructure*

The distribution of porosity in the microstructure, as represented in 3D using Fusion 360 software, is shown in Figure 4a,b for porosity levels of 56% and 46%. Distinct colors are used to visually differentiate the various microstructure phases, such as metal and oxide porosities. The overall dimension of the micrograph remains constant at 0.6 mm by 0.412 mm despite the fact that specific microstructure components vary in size and form.

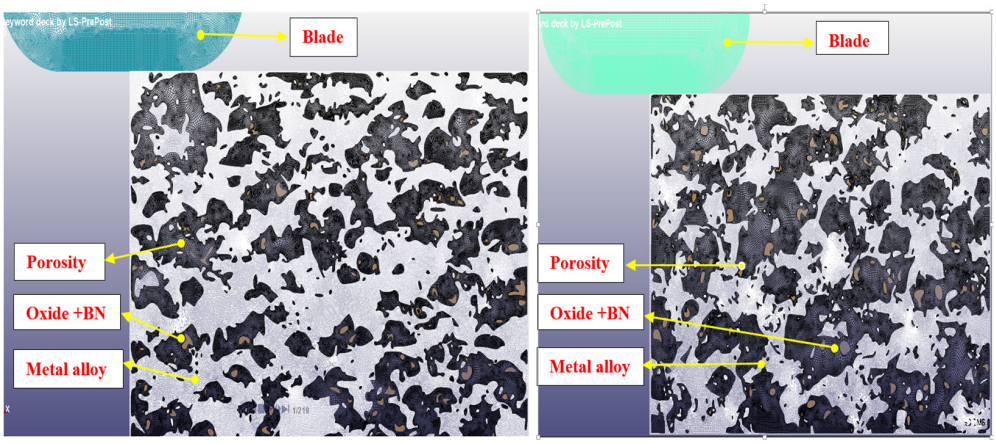


**Figure 4.** Illustrates the 3D modalities at (**a**) 56% porosity (48 HR15Y) and (**b**) 46% porosity (71 HR15Y).

The meshes for these microstructures are shown as two-dimensional surfaces, with the oxide and metal phases denoted by different colors. Five was the original size used to simulate the porosity phase components. One of the coatings had a porosity of 56% (48 HR15Y hardness), whereas the other had a porosity of 46% (71 HR15Y). They each had around 800,000 elements. The matching blade models have almost 100,000 elements. Consistency in simulation accuracy was ensured by universally applying a constant stress hexahedral 8-node solid element formulation to all components, including metal, oxide, and porosity phases.

### *2.5. Microstructure FEM Model in LS-DYNA 13.1 Software*

The metal, oxide, and porosity components in the three-dimensional model are composed of several layers. The model size is around 0.6 mm by 0.142 mm in plane. The porosity is represented discretely for continuity. With dimensions of 0.5 × 0.02 mm and a semi-circular bottom, Figure 4 shows a multi-layered 3D blade model. For the coating and blade models in the simulation setup, LS-Dyna 13.1 is used. On a turbine disc, test blades can reach speeds of up to 500 m/s at their tips. The speed at which the test specimen enters the rotor, known as the incursion rate, may be changed from 1 µm/s to 2000 µm/s. Under

normal testing settings, blade tip speeds fall between 250 and 410 m/s [51], while intrusion rates usually vary between 5 and 500 μm/s. This configuration enables a thorough examination of wear behavior under varied operating situations. A high-speed spinning wheel at a predetermined feed rate scraping a covered coupon, the test replicates the dynamic obstacles that blade tips encounter in real-world situations. After testing, the information on coating wear on the coupons and blade tips was obtained. For dynamic wear simulations, LS-Dyna 13.1 works well. Abradability, which is the ratio of coating wear to blade wear, evaluates coating performance. From reference [51], the blade oscillates at roughly from 350 to 400 m/s, which is equal to the wheel's linear velocity. Boundary conditions are used to regard the coating model's bottom surface as non-reflective in order to prevent dynamic wave reflections. Constraints are imposed on the left and bottom sides of the longer vertical surfaces under plane strain circumstances. The blade is also impacted by forward and backward displacements and velocity restrictions. For blade-length surfaces, standard maximum failure stress is applicable. The velocity statistics in Figure 5a,b, which are separated into 30 intervals, show how the MOTION command is applied to the blade's boundary, guaranteeing accurate control of the blade's location throughout the simulation.

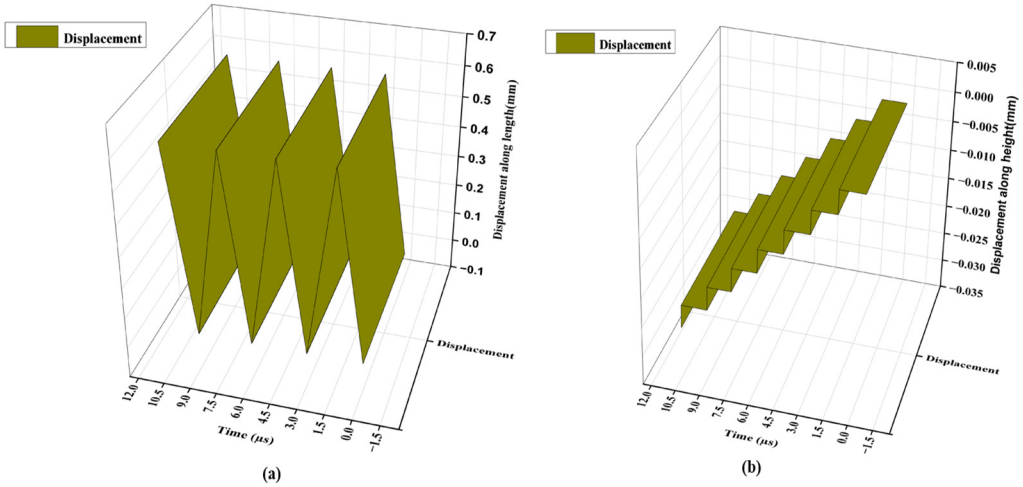


**Figure 5.** The boundary conditions that are applied to the blade in two directions: (**a**) horizontally and (**b**) vertically downward.

The Choice of Material for the Blade Modality and the Abradable Coating Is Crucial

Ti64 [34], also known as titanium alloy Ti-6Al-4V, is a high-performance material comprising 6% aluminum, 4% vanadium, and 90% titanium. Renowned for its exceptional strength-to-weight ratio, superior corrosion resistance, and thermal stability, this alloy is a cornerstone in advanced engineering applications. Its widespread use in aerospace, biomedical implants, and high-performance automotive components underscores its versatility and efficacy in withstanding extreme operational environments.

The piecewise linear plasticity (Ti64) material model, which was chosen for its simplicity and affordability, is used to model the Titanium 64 blade. Based on earlier studies, this model incorporates temperature effects at 600 °C, with stress–strain test data for Ti64 shown in Table 1 [16]. Critical inputs for the blade, such as modulus and Poisson's ratio, are listed in Table 2 and are taken from earlier research. The equivalent stress-at-failure value of 0.40 GPa for blade erosion is specified using the MAT ADD EROSION instruction, and hourglass control is consistently applied to guarantee error avoidance across all components.

**Table 1.** Blade stress vs. strain values at 600 °C [16].

| S. No | Stress (σ) GPa | Strain (ε) |
|---|---|---|
| 1 | 0 | 0 |
| 2 | 0.38 | 0.02 |
| 3 | 0.57 | 0.025 |
| 4 | 0.72 | 0.05 |
| 5 | 0.73 | 0.12 |
| 6 | 0.7 | 0.25 |
| 7 | 0.56 | 0.3 |

**Table 2.** Titanium 64 blade material properties [48].

| Property | Unit | Value |
|---|---|---|
| Density | $(kg/mm^3)$ | $4.45 \times 10^{-6}$ |
| Young's modulus | (GPa) | 114 |
| Poisson's ratio | - | 0.31 |

To model blade behavior, Material Model 24 was used, which takes advantage of piecewise linear plasticity. To take strain rate effects into account, the stress yield scaling method was used to integrate stress-strain curves into the keyword file. The quick process velocity reduced heat transmission despite substantial deformations that result in thermal softening, turning the system into an isothermal model with little temperature swings.

The dynamic yield stress is expressed as follows in LS-Dyna [45]:

$$\mu = \left(\sigma_0 + \beta E_P \varepsilon_{eff}^{p}\right)\left[1 + \left(\left(\frac{\varepsilon}{c}\right)^{\frac{1}{P}}\right)\right] \quad (1)$$

For this LS-Dyna alloy coating simulation, the kinematic plasticity material model was used. The model provides separate metal, oxide, and porosity data; this model offers distinct values for metal, oxide, and porosity, where $\sigma_Y$ represents the dynamic yield stress and density for all coating components taken from [30,31,36,37] At elevated temperatures, the yield strength decreases significantly, and the tangent modulus could drop sharply due to thermal softening. The as-sprayed samples underwent a heat treatment cycle in order to burn off the polyester in the abradable seals and attain the required porosity. The assessment of porosity in thermal spray coatings is guided by standards [58,59], which are often followed for measuring porosity in aerospace abradable coatings. These techniques usually use image processing to measure porosity percentages and microscopic examination of polished cross-sections. The application may also call for advanced non-destructive methods like X-ray computed tomography (XCT). The thorough combustion due to thermal softening often results in a reduction of 50–80% of the Young's modulus. The estimates given indicate that, based on trial simulations, the failure strain limits for metal are 2.5%, oxide is 1%, and porosity is 4%. Table 3 from [28] provides the material parameters, such as Young's modulus. Poisson's ratio for the cited coating materials, which are CoNiCrAlY–hBN–polyester and Oxide+BN, was facilitated by the exhaust system during the 3.5-h procedure, which took place at 500 °C in air. Porosity is modeled as a soft material, similar to a polymer, to guarantee convergence and allow low-range material attributes to be entered into the simulation. As stated in [29], with soft polymers influencing important characteristics like density and Young's modulus, the ideal porosity failure strain varied from 3% to 7%. A small fraction of coating components are vulnerable to strain-based failure and,

according to a few references and our estimate of the tangent modulus ($E_T$), at elevated temperatures (e.g., 600–1000 °C), the tangent modulus can drop even further.

**Table 3.** Abradable coating material properties of CoNiCrAlY–hBN–polyester [28,30,31,49,50,60].

| Material | Density (Kg/mm$^3$) | Failure Strain | Poisson's Ratio | Young's Modulus (GPa) | Yield Strength (GPa) [50] | Tangent Modulus (GPa) [50] |
|---|---|---|---|---|---|---|
| Abradable seal (CoNiCrAlY) | $3 \times 10^{-6}$ [60] | 0.025 [31] | 0.3 [28] | 140 [50] | 0.35<br>0.575<br>0.7 | 75<br>97.5<br>120 |
| | | | | 100 [50] | 0.35<br>0.575<br>0.7 | 75<br>97.5<br>120 |
| Porosity | $1 \times 10^{-6}$ [29] | 0.04 [29] | 0.33 [28] | 2.0 [29] | 0.025 | 0.1 |
| (Oxide+BN) | $3.8 \times 10^{-6}$ [49] | 0.01 [31] | 0.3 [28] | 190 [28] | 0.375 | 180 |

In order to obtain more abradability, several ideal settings may be made, and the testing parameters are changed by comprehending the impact of each individual parameter setting. Both microstructure models followed their ideal parameters. The model of the microstructure was optimized at 56 porosity and 48 HR15Y and at 46 porosity and 71 HR15Y:

1. Abradability may be obtained by varying the testing parameters, such as the yield stress point and tangent modulus while maintaining the hardness and porosity level and the Young's modulus of the seal.
2. The Young's modulus of the shroud material varies to ensure abradability, but testing factors like yield stress point and tangent modulus stay constant.

The composition and creation of both microstructures are identical; the main distinction is that they vary in porosity and hardness. The output parameter is greatly impacted by these abradable seal characteristics.

## 3. Results

### *3.1. FE. Model of Abradable Seal Following Volume Loss at 56% Porosity (48 HR15Y) and 46% Porosity (71 HR15Y) 3D Microstructure*

The blade moves according to the velocity shown in Figure 5a,b. The colors in Figure 6a,b represent distinct pore sizes and shapes in two microstructures, each of which corresponds to a particular metallurgical step. The blade stops moving after a predefined amount of time. However, the coated substance loses some of its material—specifically, metal and oxide—during this process. Even while the blade's loss is obvious, it is crucial to remember that metal and oxide are also lost throughout this process. The blade and the coated substance eventually start to separate by a little space. The simulation employs a volume fail command to ascertain the volume loss of the metal alloy and oxide shroud material as soon as the gap between the blade and seal appears. The component loss and abradability determined by the results graphs below may be identified using the graphs below.

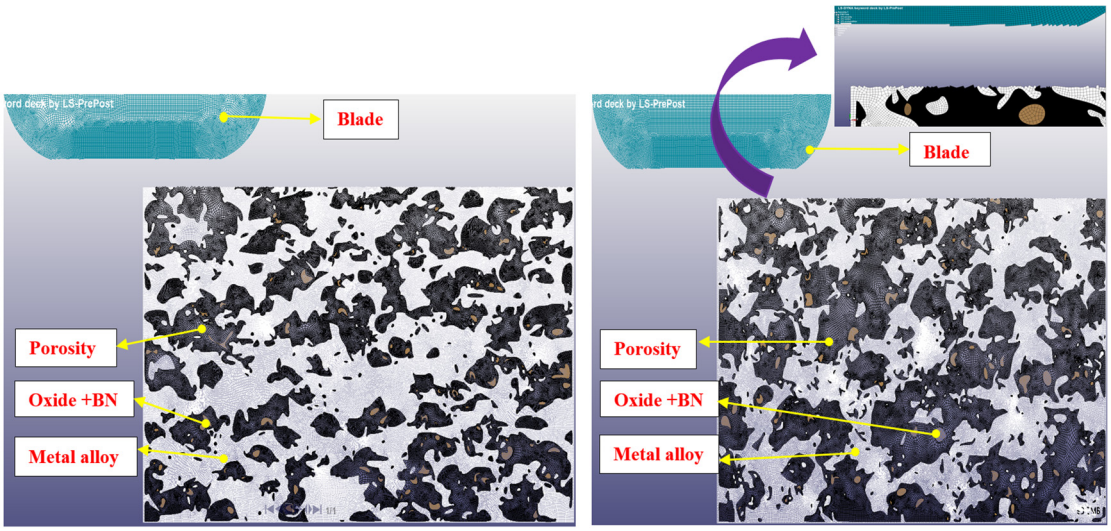


**Figure 6.** The seal's 3D microstructure after erosion: (**a**) 56% porosity (48 HR15Y) and (**b**) 46% porosity (71 HR15Y).

### *3.2. The Abradability and Erosion Findings for All Components Are Shown for a 56% Porosity (48 HR15Y) Seal with a Young's Modulus of 140 (GPa)*

The movement of the blade before it stops on the coated surface after a predetermined amount of time is shown in Figure 5a,b. Oxide layers, porosity, and metal alloys are represented by different variations of color in the microstructure. The simulation in Figure 7a shows that metal alloy and oxide are lost by the blade and abradable seal, suggesting that a small gap causes constant material loss in both.

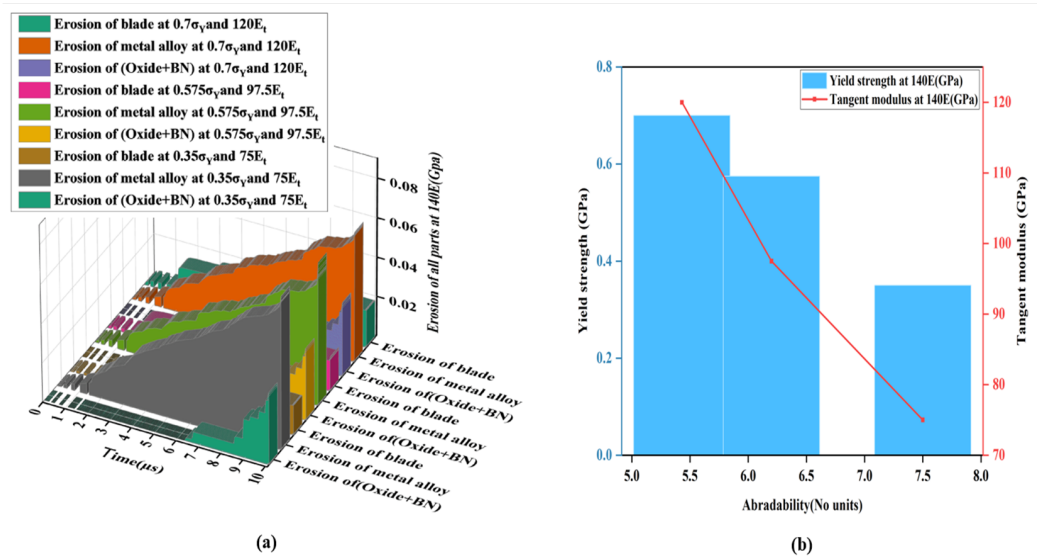


**Figure 7.** An abradable seal with a Young's modulus of 140 GPa and 56% porosity (48 HR15Y) shows (**a**) the erosion of the shroud material (blade, oxide, and metal alloy) over time and (**b**) the fluctuation of abradability with respect to yield stress and tangent modulus.

In post-simulation analysis, metal alloy, oxide, and blade volume losses are evaluated using the 'volume fail' command in the d3 plot. Metal alloy and oxide losses increase when the blade pierces the coating, finally surpassing blade loss. Blade deterioration is significantly outweighed by oxide and metal alloy erosion in coatings with 56% porosity.

The purpose of this research is to comprehend the effects of different coating and blade component material qualities on abradability. It is possible to identify the ideal parameters

for increased abradability by separating the effects of each component. A microstructure-based FEA mesh model is used in every instance. Table 3 displays the different qualities of the shroud material. The yield point stress increases incrementally from 0.35 GPa to 0.7 GPa, and the metal tangent modulus increases from 75 GPa to 120 GPa in Figure 6a. Throughout each modification, other material qualities remain constant. The metal tangent modulus and yield stress are important because changes to the Young's modulus of CoNiCrAlY at 140 GPa significantly influence its wear resistance.

Figure 7b illustrates that, although the removal rate of blade material rises and results in a large decline in the abradability number, the removal rate of shroud material (metal + oxide) stays almost constant as the shroud metal tangent modulus increases, reducing slightly owing to forced removal. Similar to this, the abradability number noticeably drops when the yield point stress level rises because the blade removal rate increases while the shroud material removal rate somewhat reduces.

### *3.3. The Abradability and Erosion Findings for All Components Are Shown for a 56% Porosity (48 HR15Y) Seal with a Young's Modulus of 100 (GPa)*

Figure 8a shows that the metal erosion rate rises with the depth of the blade penetration, resulting in a greater volume loss for metal than oxide, while oxide loss is still marginally lower than metal. Compared to metal and oxide losses, blade volume loss is also smaller. As the blade wears away the coating, the volume losses of metal, oxide, and blades increase. Data were recorded over time for a coating with 56% porosity and 48 HR15 Rockwell hardness. While the abrasion-resistant seal loses a significant amount of metal and oxide, the blade loses less volume across the whole range despite the metal and oxide losses reaching the maximum levels anticipated for the specified porosity and hardness.

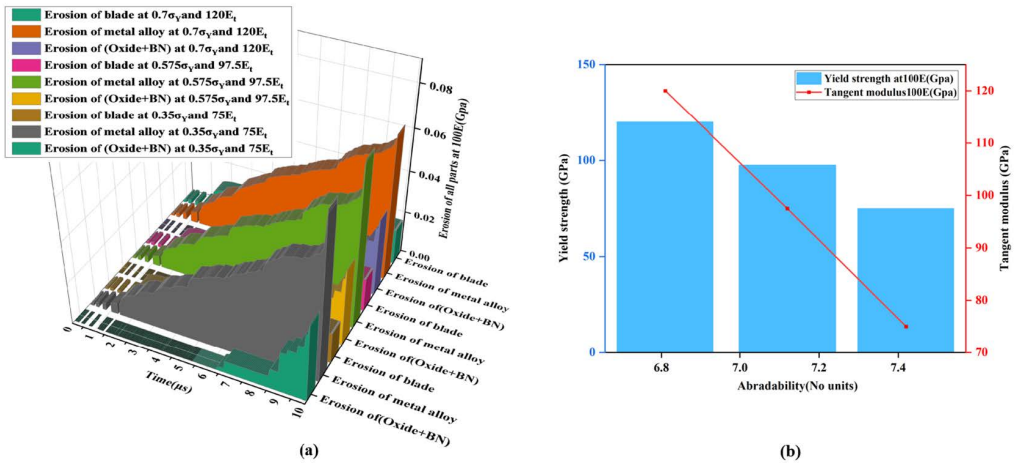


**Figure 8.** The seal, composed of CoNiCrAlY, has a Young's modulus of 100 GPa and a porosity of 56% (48 HR15Y). (**a**) Metal alloy, oxide, and blade erosion with time; (**b**) changes in abradability in relation to yield stress and tangent modulus.

The wear of the CoNiCrAlY seal at 100 GPa is shown in Figure 8b. The shroud metal's yield stress increases from 0.35 GPa to 0.7 GPa, and its tangent modulus shifts from 75 GPa to 120 GPa. The rate at which the shroud material (metal + oxide) is removed is comparatively constant as the tangent modulus of the shroud rises, with a little decline brought on by forced removal. However, when the blade's rate of material removal increases, the abradability number significantly decreases. Likewise, as the yield stress rises, the rate of removal of the shroud material somewhat drops, but the rate of removal of the blade rises, resulting in a further reduction in abradability.

Here, it was found that, in contrast to Figure 6a,b, variations in other shroud characteristics, such as hardness and porosity, had no impact on abradability. However, a

little increase in the rate of material removal from the shroud and a decrease in the rate of material removal from the blade was seen when the CoNiCrAlY seal's Young's modulus was changed from 140 GPa to 100 GPa. Table 4 illustrates how this resulted in a much higher abradability value.

**Table 4.** Abradable coating (CoNiCrAlY–hBN–polyester) erosion, blade erosion, and seal abradability for 56% porosity (48 HR15Y).

| S.no | Young's Modulus (GPa) | Yield Strength (GPa) | Tangent Modulus (GPa) | Abradable Seal (CoNiCrAlY) ($mm^3$) | (Oxide + BN) ($mm^3$) | Blade ($mm^3$) | Abradability |
|---|---|---|---|---|---|---|---|
| 1 | 140 | 0.7 | 120 | $6.62 \times 10^{-2}$ | $3.7 \times 10^{-2}$ | $1.9 \times 10^{-2}$ | 5.43 |
| | | 0.575 | 97.5 | $7.2 \times 10^{-2}$ | $3.68 \times 10^{-2}$ | $1.75 \times 10^{-2}$ | 6.2 |
| | | 0.35 | 75 | $7.8 \times 10^{-2}$ | $3.68 \times 10^{-2}$ | $1.52 \times 10^{-2}$ | 7.5 |
| 2 | 100 | 0.7 | 120 | $6.77 \times 10^{-2}$ | $3.69 \times 10^{-2}$ | $1.7 \times 10^{-2}$ | 6.81 |
| | | 0.575 | 97.5 | $7.81 \times 10^{-2}$ | $3.688 \times 10^{-2}$ | $1.6 \times 10^{-2}$ | 7.12 |
| | | 0.35 | 75 | $7.9 \times 10^{-2}$ | $3.7 \times 10^{-2}$ | $1.41 \times 10^{-2}$ | 7.42 |

### *3.4. The Abradability and Erosion Findings for All Components Are Shown for a 46% Porosity (71 HR15Y) Seal with a Young's Modulus of 140 (GPa)*

The findings show that metal alloy and oxide losses rise as the blade pierces the covering, ultimately outpacing the blade's own material loss. Blade deterioration is much outweighed by oxide and metal alloy erosion in a 46% porosity covering. Figure 9a,b also demonstrates how the rate of metal erosion increases as the blade depth increases, making it evident that the blade loss is still less than that of the metal and oxide.

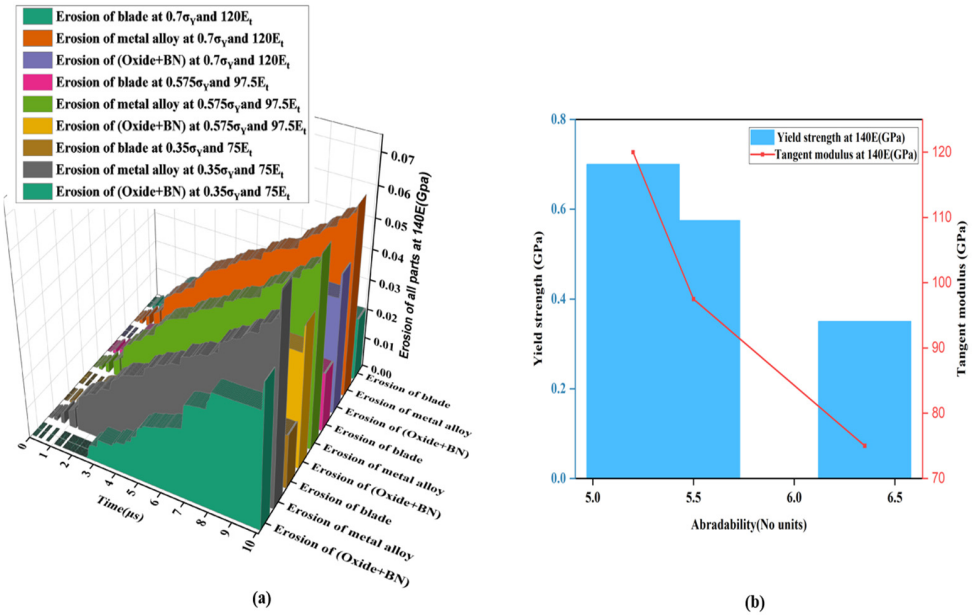


**Figure 9.** Abradable seal (CoNiCrAlY) with 46% porosity (71 HR15Y) 140 GPa Young's modulus. (**a**) Time-dependent erosion of the shroud material (blade, metal alloy, oxide); (**b**) abradability change in relation to yield stress and tangent modulus.

Both the blade and the metal and oxide components of the coating exhibit increased volume losses as the blade penetrates deeper into the coating; this is especially evident at 46% porosity and 71 HR15 Rockwell hardness. The abrasion-resistant seal's volume loss resulted in a decrease in metal and oxide, which is different from these findings. It is predicted that the blade's volume loss will exceed the expected reduction in metal and oxide loss from the abradable seal over the entire time period. Given the potential for dire

outcomes from high blade wear rates, this emphasizes the significance of blade wear in assessing abrasion-resistant seal effectiveness. Secondary damage, for instance, might arise from sudden increases in unequal force applied to the seals.

For every scenario in this investigation, a microstructure-based FEA mesh model was used, as previously mentioned. In the beginning, the parameters of the shroud material, as shown in Table 3, did not change. Figure 9a shows the modification of the tangent modulus of the shroud metal and the adjustments to the yield point stress level, as was covered in earlier talks. Notably, changing the CoNiCrAlY abradable seal's Young's modulus at 140 GPa significantly affected the abradability parameter, even while the shroud's hardness and porosity remained relatively same. Thus, only the metal tangent modulus and yield point stress were changed in this research.

Figure 9b shows that the rate of removal of the shroud material (metal + oxide) remains relatively constant when the tangent modulus and yield point stress level of the shroud metal increase, with a small decrease because of forced removal. The abradability value significantly decreases as the blade material removal rate rises in the meanwhile.

### *3.5. The Abradability and Erosion Findings for All Components for a 46% Porosity (71HR15Y) Seal with a Young's Modulus of 100 (GPa)*

Figure 10a illustrates how the metal erosion rate rises with increasing blade penetration, with metal volume loss exceeding oxide volume loss while blade loss stays below both. The volume loss of the blade rises as it penetrates further into the coating; over the whole duration, 46% porosity and 71 HR15 Rockwell hardness were noted. Although metal and oxide volume loss is noticeable in the abrasion-resistant seal, the overall volume loss of the blade over time is less than that of the metal and oxide in the abradable seal.

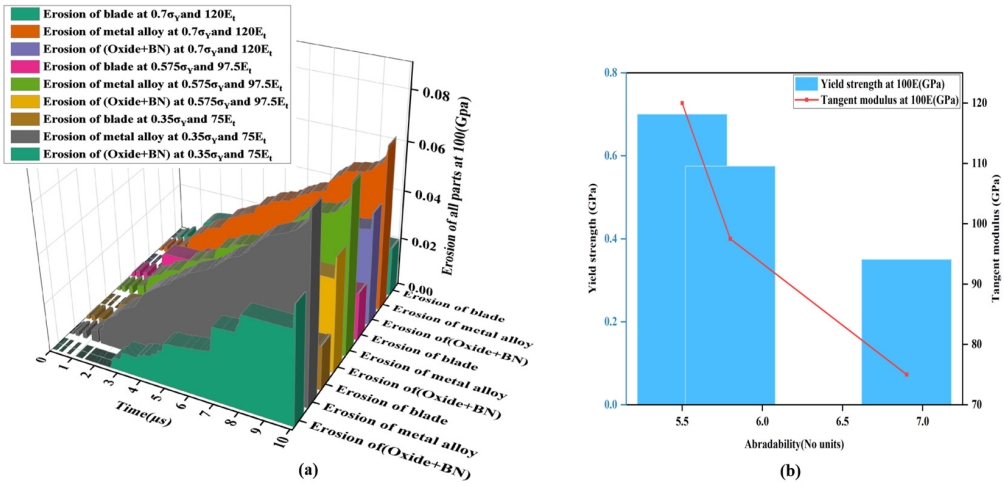


**Figure 10.** Abradable seal (CoNiCrAlY) with 46% porosity (71 HR15Y) 100 GPa Young's modulus. (**a**) Time-dependent erosion of the shroud material (blade, metal alloy, oxide); (**b**) abradability change in relation to yield stress and tangent modulus.

The (CoNiCrAlY) seal can be worn away at 100 GPa with ease, as shown in Figure 10b which also displays variations in the metal's yield point stress and tangent modulus. Due to forced removal, the removal rate of the shroud material (metal + oxide) somewhat reduces when the tangent modulus of the shroud metal rises, whereas the material removal rate of the blade increases. This causes the abradability number to decrease significantly. A further decrease in abradability results from the shroud material removal rate marginally decreasing as yield point stress increases while the blade removal rate keeps increasing.

Changes in the other characteristics of the shroud, such as its porosity and hardness, clearly have less effect on abradability than in Figure 8a,b. As seen in Table 5, however,

lowering the Young's modulus of the CoNiCrAlY seal from 140 GPa to 100 GPa makes it significantly more abradable, harder to remove the blade, and easy to remove the shroud. These scenarios vary primarily in the testing settings and the different degrees of porosity and hardness of the microstructures.

**Table 5.** Abradable coating (CoNiCrAlY–hBN–polyester) erosion, blade erosion, and seal abradability for 46% porosity (71 HR15Y).

| s.no | Young's Modulus (GPa) | Yield Strength (GPa) | Tangent Modulus (GPa) | Abradable Seal (CoNiCrAlY) ($mm^3$) | (Oxide + BN) ($mm^3$) | Blade ($mm^3$) | Abradability |
|---|---|---|---|---|---|---|---|
| 1 | 140 | 0.7 | 120 | $6.2 \times 10^{-2}$ | $4.65 \times 10^{-2}$ | $2.1 \times 10^{-2}$ | 5.2 |
| | | 0.575 | 97.5 | $6.27 \times 10^{-2}$ | $4.72 \times 10^{-2}$ | $1.98 \times 10^{-2}$ | 5.5 |
| | | 0.35 | 75 | $6.8 \times 10^{-2}$ | $4.75 \times 10^{-2}$ | $1.82 \times 10^{-2}$ | 6.35 |
| 2 | 100 | 0.7 | 120 | $6.74 \times 10^{-2}$ | $4.6 \times 10^{-2}$ | $2.03 \times 10^{-2}$ | 5.5 |
| | | 0.575 | 97.5 | $6.93 \times 10^{-2}$ | $4.69 \times 10^{-2}$ | $1.98 \times 10^{-2}$ | 5.8 |
| | | 0.35 | 75 | $7.62 \times 10^{-2}$ | $4.82 \times 10^{-2}$ | $1.83 \times 10^{-2}$ | 6.9 |

By comprehending the impact of each particular parameter, settings may be optimized to obtain more abradability. The formula for calculating abradability is as follows.

$$Abradability = \frac{Erosion\ of\ shroud\ or\ volume\ loss\ of\ shroud(Abradable\ seal(CoNicrAlY) + (Oxide + BN))}{Erosion\ of\ blade\ or\ volume\ loss\ of\ blade}$$

The blade experiences wear in minimal increments with each pass, simultaneously losing some of its material as it moves vertically downward in alternating directions, as defined by the boundary condition. In the operation, the blade continuously removes material by completing 30 passes. The volume losses for metal, oxide, and the blade may be computed separately using Figure 10 by using data from the previous 30 passes for metal and oxide volume loss and the last 30 runs for blade volume loss.

As shown in Figures 7–10, abradability increases gradually from the first to the final pass. The microstructure with 56% porosity and 48 HR15Y hardness showed higher values because it is less hard and has more holes. As can be seen in Figure 10b, the microstructure with 46% porosity and 71 HR15Y has reduced abradability on the 30th pass because of its higher hardness values and lower porosity.

Abradability trends for the 30th pass for both APS1 and APS2 coatings are shown in Tables 4 and 5, which show rising and falling abradability trends for varying porosity and hardness levels.

Reference [27] provided some of the experimental data in Table 6, including bond strength, erosion rate, porosity, and hardness. In this research, an FEA model of the testing environment for the rub rig was made, and LS-Dyna simulation was used to find an attribute called "abradability". The trend in abradability variation does match the trend in hardness and other experimental parameters, validating the modeling methodology.

**Table 6.** Comparison of abradability with experimental properties [27].

| S. No | Property | Case 1 | Case 2 |
|---|---|---|---|
| 1 | Bond strength (Mpa) | 4.8 | 12.5 |
| 2 | Erosion rate (μm/s) | 5.9 | 2.2 |
| 3 | Wear of blade (μm) | 0 | 100 |
| 4 | Wear of abradable seal (μm) | 1100 | 900 |
| 5 | Porosity (%) | 56 | 46 |
| 6 | Rockwell hardness (HR15Y) | 48 | 71 |
| 7 | Abradability | 6.81 | 5.5 |

### *3.6. Evaluation of Abradability in Relation to Experiment Findings*

#### 3.6.1. Evaluation of Coating Abradability in Relation to Hardness and Porosity

Figure 11a illustrates the connection between abradability, coating porosity, and coating hardness. A clear correlation was seen as abradability increased from 5.5 to 6.81 as porosity increased from 46% to 56%. In order to create porosity, abradable seals are composite materials made of a metal matrix, a ceramic phase, and a polymer or self-lubricating non-metal phase. Polyester was eliminated by a heat treatment to obtain the required porosity. The relationship between abradability and hardness is inverse, abradability increased as hardness dropped from 71 HR15Y to 48 HR15Y. Because the material was more durable, increased hardness led to more damage to the blade.

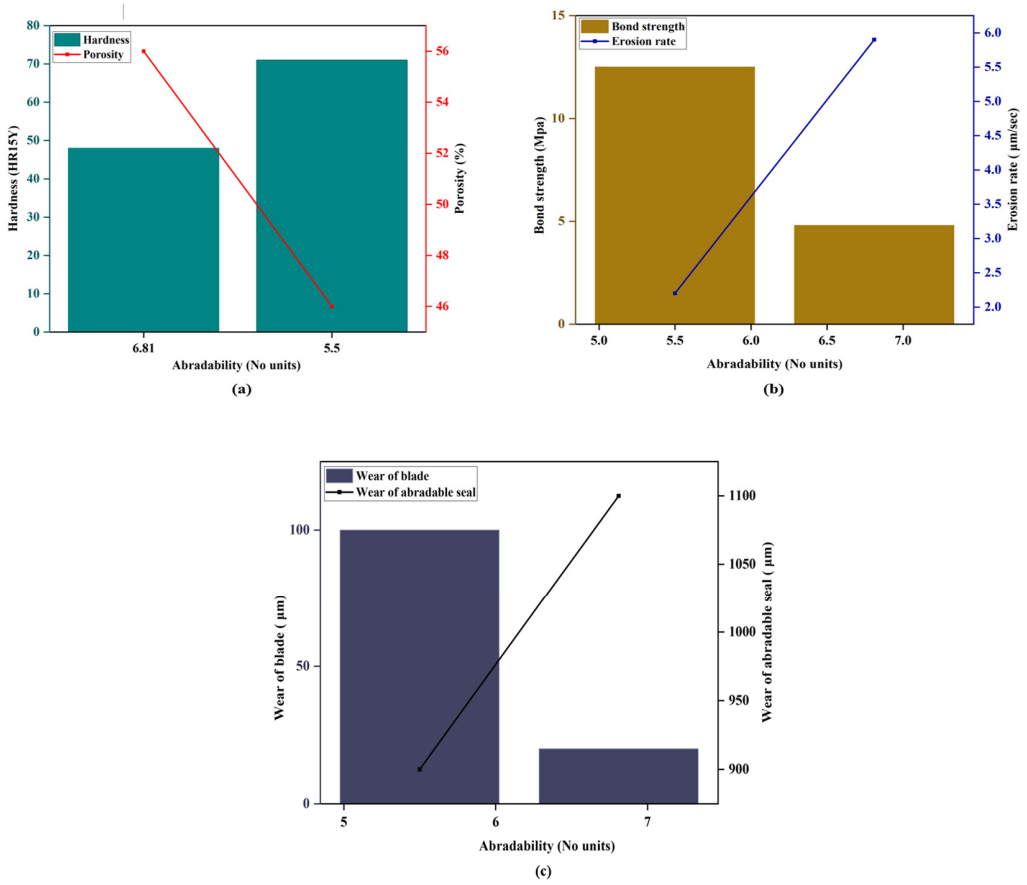


**Figure 11.** (**a**) The porosity percentage and Rockwell hardness have an impact on the variance in abradability; (**b**) bond strength and erosion rate affect abradability variation; (**c**) variability in abradability is correlated with seal and blade wear.

#### 3.6.2. Evaluation of Coating Abradability in Relation to Erosion Rate and Bond Strength

The link between bond strength, erosion rate, and coating abradability is shown in Figure 11b. Abradability in the ranges of hardness and porosity under study exhibited a linear connection with erosion rate, rising from 5.5 to 6.81. Cohesion was the mechanism of failure for all microstructures. Greater bond strength decreased abradability, indicating an inverse linear connection, whereas a lower bond strength was associated with greater abradability values. By striking the correct balance between wear resistance and abradability, abradable coatings safeguard the fan and compressor components of aircraft engines. By lessening the harm that tiny particles wreak during takeoffs and landings, they accomplish this.

#### 3.6.3. Evaluation of Coating Abradability in Relation to Blade and Abradable Seal Wear Results

The connection between abradability numbers, seal wear depth, and blade wear is shown in Figure 11c. While seal wear rises proportionately with abradability, blade wear falls inversely with increasing abradability. Blade wear is the key component of abradable seal performance, as more abradability causes more seal wear but less blade wear. Unbalanced forces and further seal damage are two negative effects of excessive blade wear. This demonstrates how crucial it is to use the appropriate abradable coatings to reduce blade wear while maintaining the functionality of seals.

#### 3.6.4. Variability in Parameters and Their Impact on Abradability

For checking the effect of variation of material properties on abradability, and also their interaction with each other, parametric analysis was performed using a simple design of experiment involving one particular 3D model. One important thing was that, while analyzing all these cases, most of the parameter settings were kept constant while one parameter was varied. Response surface analysis was performed, and the plots were generated. These plots show the variation of a single parameter with respect to another with respect to the output, i.e., abradability. As shown in Figure 12a, lower yield strength and higher modulus of the coating material give a higher abradability ratio. Figure 12b shows that the lower failure strain and higher modulus of the coating material give a higher abradability ratio. Figure 12c shows that the higher strength of the blade material and higher modulus of the coating materials yield a higher abradability ratio. Figure 12d shows that the lower porosity level of the coating material and higher modulus of the coating material yields a higher abradability ratio. Figure 13a shows that a higher strength of the blade material and a lower yield strength of the coating material yields a higher abradability ratio. Figure 13b shows that any porosity level of the coating material yields the same abradability ratio at a lower yield strength of the coating material. Figure 13c shows that the lower failure strain and the lower yield strength of the coating material yield a higher abradability ratio. Figure 13d shows that, at any level of blade strength, a lower failure strain coating material shows a higher abradability ratio.

The simulation findings indicate that 3D finite element analysis (FEA) models based on microstructure pictures are an effective technique for understanding how objects wear down under rapid loading and unloading. In assessing the performance of abradable coatings, this novel approach shows great promise and provides a route to more sophisticated prediction capabilities.

The ultimate objective is to refine this technique such that the microstructural picture may be utilized to forecast the degrading rate of a coating. Without requiring extensive physical testing, this would provide a quick and precise method of performance guessing. By making the analytical procedure simpler, this method helps expedite the assessment of recently created coatings.

Furthermore, adding a database-driven structure might make the process more adaptable. Having a robust database with extensive data sets on a wide variety of coatings would improve the accuracy of predicting the behavior of unknown coatings. The process is made more effective by combining data-driven predictions and simulations, which also makes it a potent tool for developing and applying abradable coatings in a variety of technical fields.

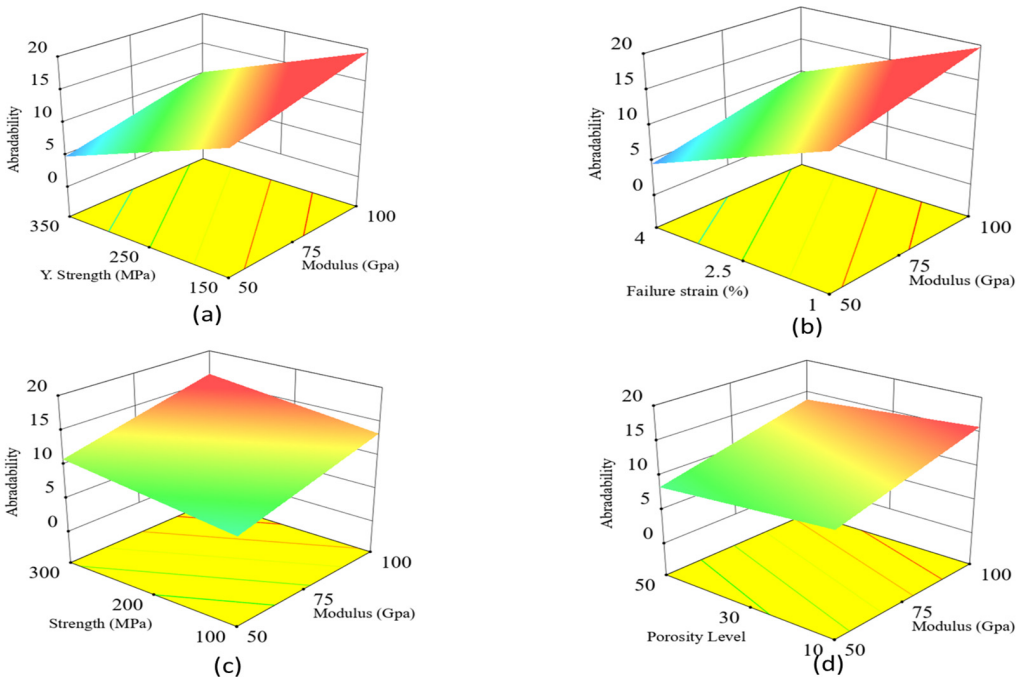


**Figure 12.** Response surface plots: (**a**) modulus vs. yield strength; (**b**) modulus vs. failure strain; (**c**) blade strength vs. modulus; (**d**) porosity level vs. modulus.

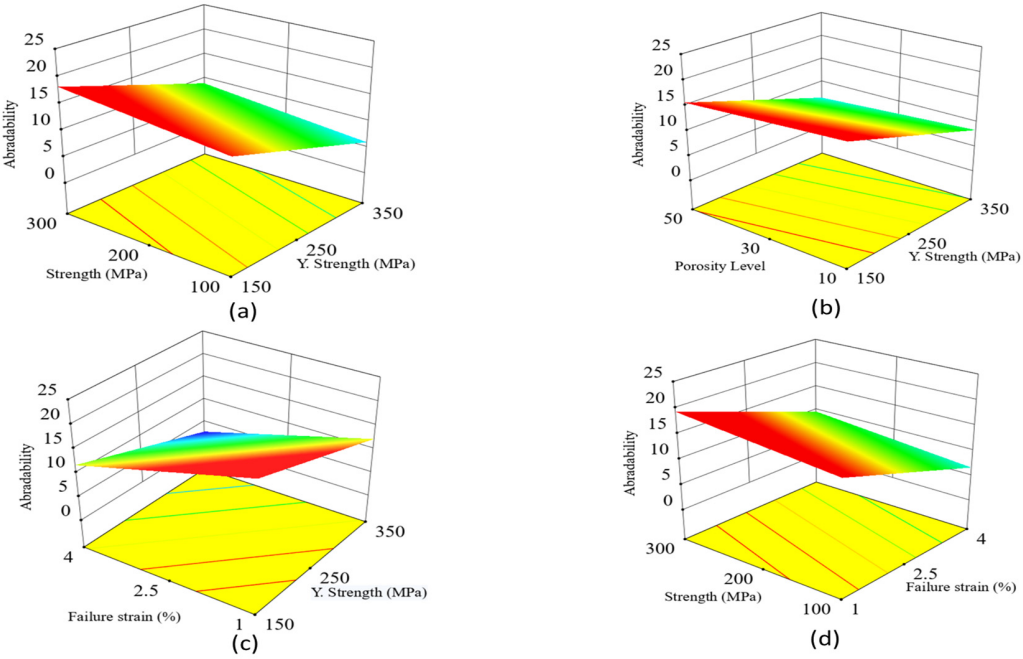


**Figure 13.** Response surface plots: (**a**) blade strength vs. yield strength; (**b**) porosity level vs. yield strength; (**c**) failure strain vs. yield strength; (**d**) blade strength vs. failure strain.

## 4. Conclusions

The methods used in this study allowed for the development of optimum abradable formulations, microstructure modeling, and efficient simulation of coating deterioration. By employing LS-Dyna-based simulated rub rig testing, the wear behavior of coatings that may be abraded was investigated. It focused on the relationships between the coatings' appearance and the concentrations of metals, oxides, and voids. These differences were associated with important output metrics, such as overall abradability, blade wear, and abradable seal wear. Coatings such as CoNiCrAl–BN polyester were examined using

microstructure photos, and rigorous modeling, meshing, and refinement procedures were used to create sophisticated 3D finite element models.

Simulations showed that, under certain circumstances, the shroud material degraded more quickly and had improved abradability. Abradability decreased as the seal's porosity and hardness increased, although it exhibited an inverse connection with yield strength, tangent modulus, and other characteristics. With erosion components of the shroud changing linearly over time, the CoNiCrAl–BN polyester coating showed slower wear rates than other coatings. To achieve these outcomes, the microstructure models that performed best at 46% porosity with 71 HR15Y and 56% porosity with 48 HR15Y were used.

1. Abradability was achieved by varying parameters such as yield stress and tangent modulus while maintaining consistent hardness, porosity, and Young's modulus of the seal. Additionally, changes to the shroud material's Young's modulus enhanced abradability, provided that yield stress and tangent modulus remained constant;
2. To determine the input parameters that alter coatings' abradability and quantify the impact of those factors on the final product—abradability—microstructure-based FEA model analysis was used;
3. How the output is affected by the primary parameters and how they interact was studied;
4. Setting the coating processing settings to attain the ideal composition and qualities will be made much easier by this research;
5. This will make it possible to apply abradabable coatings on high-pressure compressor shrouds, which will boost engine efficiency;
6. The viability of abradable coatings in high-pressure turbine zones is being investigated using a similar idea.
7. Higher degrees of porosity are shown to increase erosion rate and abradability. On the other hand, abradability falls with increasing bond strength and hardness. Additionally, if coating wear increases or blade wear decreases the abradability number increases, indicating a balance between durability and material removal in coating performance.

The microstructure composition and fabrication methods were identical, with differences arising only in porosity and hardness. These characteristics significantly influenced the output performance of the abradable seal. This demonstrates the importance of tailoring microstructural properties and testing parameters to optimize wear behavior and enhance the functional efficiency of abradable coatings in engineering applications.

In the future, abradability will be predicted using high-resolution SEM pictures, and the attributes and performance of any unknown coating composition will be predicted using the proposed simulation technique by only looking at and utilizing the microstructure image.

**Author Contributions:** Methodology, A.K.A.; Software, A.K.A.; Validation, A.K.A.; Formal analysis, A.K.A.; Investigation, A.K.A.; Resources, C.L.; Data curation, C.L.; Writing—review & editing, P.J.; Visualization, C.L.; Supervision, P.J.; Project administration, P.J. All authors have read and agreed to the published version of the manuscript.

**Funding:** This research received no external funding.

**Data Availability Statement:** Data will be provided on request.

**Conflicts of Interest:** The authors declare no conflicts of interest.

## References

1. Boyce, M.P. *Gas Turbine Engineering Handbook*; Elsevier: Amsterdam, The Netherlands, 2011.
2. Wallis, A.M.; Denton, J.D.; Demargne, A.A.J. The Control of Shroud Leakage Flows to Reduce Aerodynamic Losses in a Low Aspect Ratio, Shrouded Axial Flow Turbine. In Proceedings of the Turbo Expo: Power for Land, Sea, and Air, Munich, Germany, 8–11 May 2000; American Society of Mechanical Engineers: New York, NY, USA, 2000; Volume 78545, p. V001T03A046.

3. Michael, L.N.; Gretchen, L.G.; Robert, L.B.; Yvonne, D.K.; Sharon, S.P.; Chris, J.B.; Robert, B.S.; Alberto, A. *The Widest Practicable Dissemination: The NASA Technical Report Server*; NASA: Washington, DC, USA, 1995.
4. Melcher, K.J.; Kypuros, J.A. Toward a Fast-Response Active Turbine Tip Clearance Control. In Proceedings of the 16th International Symposium on Airbreathing Engines, Cleveland, OH, USA, 31 August–5 September 2003.
5. Steinetz, B.M.; Hendricks, R.C.; Munson, J. *Advanced Seal Technology in Meeting Next Generation Engine Goals*; NASA/TM-1998-206961, AVT-PPS Paper; NASA: Washington, DC, USA, 1998.
6. Dorfman, M.; Erning, U.; Mallon, J. Gas Turbines Use 'Abradable'Coatings for Clearance-Control Seals. *Seal. Technol.* **2002**, *2002*, 7–8. [CrossRef]
7. Schmid, R.K.; Ghasripoor, F.; Dorfman, M.; Wei, X. An Overview of Compressor Abradables. In Proceedings of the ITSC 2000, Montreal, QC, Canada, 8–11 May 2000; ASM International: Materials Park, OH, USA.
8. Novinski, E.R. The Design of thermal sprayed abradable seal coating for gas turbine engines. In Proceedings of the ITSC 1991, Pittsburg, PA, USA, 4–10 May 1991; Bernecki, T.F., Ed.; ASM International: Materials Parck, OH, USA, 1991.
9. Basu, B.; Kalin, M. *Tribology of Ceramics and Composites: A Materials Science Perspective*; John Wiley & Sons: Hoboken, NJ, USA, 2011.
10. Davim, J.P. *Wear of Advanced Materials*; John Wiley & Sons: Hoboken, NJ, USA, 2013.
11. Borel, M.O.; Nicoll, A.R.; Schla, H.W.; Schmid, R.K. The Wear Mechanisms Occurring in Abradable Seals of Gas Turbines. *Surf. Coat. Technol.* **1989**, *39*, 117–126. [CrossRef]
12. Carter, T.J. Common Failures in Gas Turbine Blades. *Eng. Fail. Anal.* **2005**, *12*, 237–247. [CrossRef]
13. Emanuelson, R.C.; Witherell, W.F. Abradable Coating. US Patent 3,413,136, 26 November 1968.
14. Shi, J.; Li, L.; Freeman, T.J. Abradable Coatings for High-Performance Systems. U.S. Patent US10900371B2, 26 January 2021.
15. Berndt, C.C.; Khor, K.A.; Lugscheider, E.F. Thermal Spray 2001: New Surfaces for a New Millenium. In Proceedings of the 2nd International Thermal Spray Conference, Singapore, 28–30 May 2001; ASM International: Almere, The Netherlands, 2001.
16. Hou, X.; Liu, Z.; Wang, B.; Lv, W.; Liang, X.; Hua, Y. Stress-Strain Curves and Modified Material Constitutive Model for Ti-6Al-4V over the Wide Ranges of Strain Rate and Temperature. *Materials* **2018**, *11*, 938. [CrossRef] [PubMed]
17. Rathmann, U.; Olmes, S.; Simeon, A. Sealing Technology: Rub Test Rig for Abrasive/Abradable Systems. In Proceedings of the Turbo Expo: Power for Land, Sea, and Air, Montreal, QC, Canada, 14–17 May 2007; Volume 47942, pp. 223–228.
18. Xiao, J.; Chen, Y.; Chen, D.; Tian, J.; Ouyang, H.; Wang, A. Interactions between Blades and Abradable Coatings: A Numerical Approach Considering Geometrical Nonlinearity. *Int. J. Mech. Sci.* **2021**, *191*, 106052. [CrossRef]
19. Faraoun, H.I.; Grosdidier, T.; Seichepine, J.-L.; Goran, D.; Aourag, H.; Coddet, C.; Zwick, J.; Hopkins, N. Improvement of Thermally Sprayed Abradable Coating by Microstructure Control. *Surf. Coat. Technol.* **2006**, *201*, 2303–2312. [CrossRef]
20. Faraoun, H.-I.; Seichepine, J.-L.; Coddet, C.; Aourag, H.; Zwick, J.; Hopkins, N.; Sporer, D.; Hertter, M. Modelling Route for Abradable Coatings. *Surf. Coat. Technol.* **2006**, *200*, 6578–6582. [CrossRef]
21. Klusemann, B.; Hortig, C.; Svendsen, B. Modeling and Simulation of the Microstructural Behaviour in Thermal Sprayed Coatings. *Proc. Appl. Math. Mech.* **2009**, *9*, 421–422. [CrossRef]
22. Bolelli, G.; Candeli, A.; Koivuluoto, H.; Lusvarghi, L.; Manfredini, T.; Vuoristo, P. Microstructure-Based Thermo-Mechanical Modelling of Thermal Spray Coatings. *Mater. Des.* **2015**, *73*, 20–34. [CrossRef]
23. Nayebpashaee, N.; Seyedein, S.H.; Aboutalebi, M.R.; Sarpoolaky, H.; Hadavi, S.M.M. Finite Element Simulation of Residual Stress and Failure Mechanism in Plasma Sprayed Thermal Barrier Coatings Using Actual Microstructure as the Representative Volume. *Surf. Coat. Technol.* **2016**, *291*, 103–114. [CrossRef]
24. Klusemann, B.; Denzer, R.; Svendsen, B. Microstructure-Based Modeling of Residual Stresses in WC-12Co-Sprayed Coatings. *J. Therm. Spray Technol.* **2012**, *21*, 96–107. [CrossRef]
25. Sheng, L.; Xiao, Y.; Jiao, C.; Du, B.; Li, Y.; Wu, Z.; Shao, L. Influence of Layer Number on Microstructure, Mechanical Properties and Wear Behavior of the TiN/Ti Multilayer Coatings Fabricated by High-Power Magnetron Sputtering Deposition. *J. Manuf. Process.* **2021**, *70*, 529–542. [CrossRef]
26. Zemlianov, A.; Balokhonov, R.; Romanova, V.; Gatiyatullina, D. The Influence of Bi-Layer Metal-Matrix Composite Coating on the Strength of the Coated Material. *Procedia Struct. Integr.* **2022**, *35*, 181–187. [CrossRef]
27. Irissou, E.; Dadouche, A.; Lima, R.S. Tribological Characterization of Plasma-Sprayed CoNiCrAlY-BN Abradable Coatings. *J. Therm. Spray Technol.* **2014**, *23*, 252–261. [CrossRef]
28. Aussavy, D. Processing Characterization and Modeling of Thermomechanical Properties of Threee Abradable Coatings: NiCrAl-Bentonite, CoNiCrAlY-BN-Polyester, and YSZ-Polyester. Ph.D. Thesis, Université de Technologie de Belfort-Montbeliard, Sevenans, France, 2016.
29. Mittal, V. *High Performance Polymers and Engineering Plastics*; John Wiley & Sons: Hoboken, NJ, USA, 2011.
30. Jadhav, P. Abradable Coatings: Design through Microstructure Based Models. *Mater. Today Proc.* **2022**, *62*, 7353–7357. [CrossRef]
31. Azmeera, A.K.; Jadhav, P.; Lande, C. Microstructure Image-Based Finite Element Methodology to Design Abradable Coatings for Aero Engines. *Aerospace* **2023**, *10*, 873. [CrossRef]

32. Huang, J.; Xueqiang, C.A.O.; Wenbo, C.; Xiaojun, G.U.O.; Min, L.I.; Wenjun, W.; Shujuan, D.; Li, L.I.U.; Meizhu, C. A Comprehensive Review of Thermally Sprayed Abradable Sealing Coatings: Focusing on Abradability. *Chin. J. Aeronaut.* **2024**, *37*, 1–25. [CrossRef]
33. Bertuol, K.; Rivadeneira, F.R.; Nair, R.B.; Barnett, B.; Moreau, C.; Stoyanov, P. Influence of hBN on the Abradable Performance of AlSi-Based Coatings: Bridging the Gap between Tribological Assessment and Abradability Testing. *Surf. Coat. Technol.* **2024**, *489*, 131060. [CrossRef]
34. Volpe, E.; Motyka, E.; Roeseler, S.; Plessinger, R.; Noyes, T.; Kweder, J. Using Simultaneous Differential Scanning Calorimetry and Thermogravimetric Analysis to Develop Braze Processes for Porous FELTMETAL$^{TM}$ Abradable Seal Material. In Proceedings of the Turbo Expo: Power for Land, Sea, and Air, London, UK, 24–28 June 2024; American Society of Mechanical Engineers: New York, NY, USA, 2024; Volume 88018, p. V009T17A024.
35. Monteiro, B.; Simões, S. Recent Advances in Hybrid Nanocomposites for Aerospace Applications. *Metals* **2024**, *14*, 1283. [CrossRef]
36. Murthy, J.K.N.; Venkataraman, B.; Lakshmi, G.; Ramakrishna, M. Development of Tribological Coatings for Aerospace and Missile Applications. *Def. Sci. J.* **2023**, *73*, 212–219. [CrossRef]
37. Cheng, J.; Hu, X.; Joost, W.; Sun, X. Micro–Macro Finite Element Modeling Method for Rub Response in Abradable Coating Materials. *J. Mater. Sci.* **2024**, *59*, 4934–4947. [CrossRef]
38. Cui, Y.; Yue, Z.; Guo, M.; Wang, C.; Jiao, J.; Cheng, L. Microstructure and phase correlation of DySZ-Polyester abradable seal coating after thermal exposure. *Mater. Today Commun.* **2023**, *36*, 106641. [CrossRef]
39. Gao, S.; Xue, W.; Duan, D.; Li, S.; Zheng, H. Effect of thermal–physical properties on the abradability of seal coating under high-speed rubbing condition. *Wear* **2018**, *394*, 20–29. [CrossRef]
40. Soltani, R.; Heydarzadeh-Sohi, M.; Ansari, M.; Afsari, F.; Valefi, Z. Effect of APS process parameters on high- temperature wear behavior of nickel–graphite abradable seal coatings. *Surf. Coat. Technol.* **2017**, *321*, 403–408. [CrossRef]
41. Martinet, B.; Cappella, A.; Philippon, S.; Montebello, C. Effect of temperature on wear mechanisms of an aluminium-based abradable coating for aircraft engines after a dynamic interaction with a Ti6Al4V blade. *Wear* **2020**, *446*, 203202. [CrossRef]
42. Kang, Y.; Chen, L.; Li, C.J.; Yang, G.J. Porous spheres enabling excellent high-temperature abradability and long lifetime for abradable seal coating. *J. Eur. Ceram. Soc.* **2024**, *44*, 1721–1732. [CrossRef]
43. Tong, Y.Q.; Shi, Q.S.; Liu, M.J.; Li, G.R.; Li, C.J.; Yang, G.J. Lightweight epoxy-based abradable seal coating with high bonding strength. *J. Mater. Sci. Technol.* **2021**, *69*, 129–137. [CrossRef]
44. Yan, H.; Yu, Y.; Song, Y.; Lei, B.; Ni, Y.; Tang, A.; Li, Y. An abradable and anti-corrosive CuAl-Ni/C seal coating for aero-engine. *Chem. Eng. J.* **2023**, *474*, 145665. [CrossRef]
45. Zhang, B.; Marshall, M. Investigating material removal mechanism of Al-Si base abradable coating in labyrinth seal system. *Wear* **2019**, *426*, 239–249. [CrossRef]
46. Mohammad, F.; Mudasar, M.; Kashif, A. Criteria for abradable coatings to enhance the performance of gas turbine engines. *J. Mater. Sci. Metall.* **2021**, *2*, 1–7.
47. Silva, M.; Tantot, N.; Selezneff, S.; Walsh, M.; Nyatando, R.; Johann, E.; Kando, A. Advanced Aero-Engines Technology Enablers: An Overview of the European Project E-BREAK. *Turbo Expo Power Land Sea Air* **2016**, *49682*, V001T01A015.
48. Tüfekci, M. Performance Evaluation Analysis of Ti-6Al-4V Foam Fan Blades in Aircraft Engines: A Numerical Study. *Compos. Part C Open Access* **2023**, *12*, 100414. [CrossRef]
49. Gialanella, S.; Malandruccolo, A. Superalloys. In *Aerospace Alloys*; Topics in Mining, Metallurgy and Materials Engineering; Springer International Publishing: Cham, Switzerland, 2020; pp. 267–386. ISBN 978-3-030-24439-2.
50. Krenkel, W. *Ceramic Matrix Composites: Fiber Reinforced Ceramics and Their Applications*; John Wiley & Sons: Hoboken, NJ, USA, 2008.
51. Wilson, S. Thermally Sprayed Abradable Coating Technology for Sealing in Gas Turbines. In Proceedings of the 6th International Conference on the Future of Gas Turbine Technology, Brussels, Belgium, 17–18 October 2012.
52. Metco, O. *Rapid Validation of Turbomachinery Abradable Systems Using Oerlikon Metco's Rub-Test Facility*; SF-0029.0–Abradable Testing; Oerlikon: Zürich, Switzerland, 2020.
53. LS-DYNA® Theory Manual. Available online: https://ftp.lstc.com/anonymous/outgoing/jday/manuals/DRAFT_Theory.pdf (accessed on 27 June 2024).
54. Metco, O. *Material Product Data Sheet: Nickel Chromium Aluminum Yttrium (NiCrAlY) Powder for Thermal Spray*; Oerlikon Metco: Westbury, NY, USA, 2014; pp. 1–6.
55. Sporer, D.; Dorfman, M.; Xie, L.; Refke, A.; Giovannetti, I.; Giannozzi, M. Processing and Properties of Advanced Ceramic Abradable Coatings. In Proceedings of the Thermal Spray 2007: Global Coating Solutions, Beijing, China, 14–16 May 2007; pp. 495–500.
56. Oerlikon-Metco. 2014. Improve Efficiency and Reduce Emissions with High Pressure Turbine Abradable Coatings Industrial Gas. Available online: https://www.oerlikon.com/ecoma/files/SF-0016.1_Steam_Turbine_Abradables_EN.pdf?download=true (accessed on 5 October 2024).

57. Bidmeshki, C. Microstructural, Mechanical, and Tribological Evaluation of Thermally Sprayed Wear-Resistant Coatings for Aerospace Applications. Ph.D. Thesis, Concordia University, Montreal, QC, Canada, 2023.
58. Pawlowski, L. *The Science and Engineering of Thermal Spray Coatings*; John Wiley & Sons: Hoboken, NJ, USA, 2008.
59. *E2109-01*; Standard Test Methods for Determining Area Percentage Porosity in Thermal Sprayed Coatings. ASTM International: West Conshohocken, PA, USA, 2014.
60. Material Product Data Sheet CoNiCrAlY-BN/Polyester Abradable Thermal Spray Powders. Available online: https://www.google.com/search?q=Material+Product+Data+Sheet%0D%0ACoNiCrAlY (accessed on 5 October 2024).